Applied Surface Science 315 (2014) 490–498

Contents lists available at ScienceDirect

Applied Surface Science

journal homepage: www.elsevier.com/locate/apsusc

Au and Pd nanoparticles supported on CeO_2, TiO_2, and Mn_2O_3 oxides

P.A.P. Nascente[a,*], S.S. Maluf[a], C.R.M. Afonso[a], R. Landers[b], A.N. Pinheiro[c], E.R. Leite[c]

[a] Federal University of Sao Carlos, Department of Materials Engineering, Sao Carlos, SP, Brazil
[b] State University of Campinas, Institute of Physics, Department of Applied Physics, Campinas, SP, Brazil
[c] Federal University of Sao Carlos, Department of Chemistry, Sao Carlos, SP, Brazil

ARTICLE INFO

Article history:
Received 17 December 2013
Received in revised form 24 March 2014
Accepted 13 April 2014
Available online 21 April 2014

Keywords:
Nanostructures
Oxides
Sol–gel growth
X-ray photoelectron spectroscopy
Transmission electron microscopy

ABSTRACT

Gold and palladium nanoparticles were incorporated on CeO_2, TiO_2, and Mn_2O_3 supports prepared by a sol–gel method. The samples were characterized by X-ray diffraction (XRD), X-ray photoelectron spectroscopy (XPS), energy dispersive spectroscopy (EDS), transmission electron microscopy (TEM), high resolution TEM (HRTEM), scanning TEM (STEM) in high angle annular dark field mode (HAADF), and energy filtered TEM (EFTEM) using electron energy loss spectroscopy (EELS). The XRD diffractograms presented sharp and intense peaks indicating that the samples are highly crystalline, but it did not detected any peak corresponding to Au or Pd phases. This indicates that the Au and Pd NPs were incorporated into the structures of the oxides. It was not possible to obtain an Au 4f spectrum for Au/Mn_2O_3 due to an overlap with the Mn 3p spectrum. The XPS Au 4f spectra for Au/CeO_2 and Au/TiO_2 present negative chemical shifts that could be attributed to particle-size-related properties. The XPS Pd 3d spectra indicate that for both CeO_2 and TiO_2 substrates, the Pd NPs were in the metallic state, while for the Mn_2O_3 substrate, the Pd NPs were oxidized. The HRTEM results show the formation of nanocrystalline oxides having particles sizes between 50 and 200 nm. TEM micrographs show that the addition of Au caused the formation of Au clusters in between the CeO_2 NPS, formation of Au NPs for the TiO_2 support, and homogeneous distribution of Au clusters for the Mn_2O_3 support. The addition of Pd yielded a homogeneous dispersion throughout the CeO_2 and TiO_2, but caused the formation of Pd clusters for the Mn_2O_3 support.

1. Introduction

New generation advanced nanoparticle materials exhibit unique physical, magnetic, optical, surface structural properties with potential in developing new technologies, techniques, and improvement of old methods/processes in catalysis, sensor technology, and fabrication of nanodevices [1,2]. The transition metal oxide nanoparticles represent a broad class of materials that have been investigated extensively due to their interesting catalytic, electronic, and magnetic properties, and wide scope of potential applications, such as magnetic resonance imaging (MRI) [3], solar cells [4], and heterogeneous catalysis [5–8].

Cerium oxide has been reported as an active support for nanostructured gold, platinum, and palladium catalysts for water–gas shift reaction and other industrial applications [9–11]. Titanium oxide has been extensively used as support for metallic nanoparticles (NPs) such as palladium for heterogeneous catalytic applications in both oxidation [9–12] and hydrogenation reactions [13–16]. Manganese oxides (MnO, Mn_2O_3, and Mn_3O_4) have long been used as highly active, durable, and low cost catalysts for the combustion of various volatile organic substances or hydrocarbons [17–19].

Catalysis is a phenomenon of significant fundamental research and important practical applications in a variety of fields such as chemistry, physics, materials science, and environmental science. Nanoparticles of metal and metal oxide can enhance catalytic performance over conventional catalysts, by having controlled particle size, high surface area, and more densely populated unsaturated surface coordination sites [1,2].

Gold catalysts were not widely used due to the electronic configuration of the noble metals, which is usually accompanied by very low activities [20]. This situation has changed in recent years with the discovery of the catalytic activity of gold nanoparticles [21]. Gold catalysts have recently attracted growing interest due to their potential for many reactions of both industrial and environmental importance. The most remarkable catalytic properties of supported gold have been first obtained for the reaction of CO oxidation at sub ambient temperature by Haruta et al. [22,23]. Gold can also be active in various other reactions, such as selective hydrogenation, water–gas shift, reduction of NO with hydrocarbons, epoxidation of

* Corresponding author. Tel.: +55 1633518528; fax: +55 1633611160.
E-mail address: nascente@ufscar.br (P.A.P. Nascente).

http://dx.doi.org/10.1016/j.apsusc.2014.04.090
0169-4332/

propylene, CO and CO_2 hydrogenation, and in reactions involving halogens [24].

In this work, nanoparticles of gold and palladium have been added onto CeO_2, TiO_2 and Mn_2O_3 supports and then have been characterized by X-ray diffraction (XRD), X-ray photoelectron spectroscopy (XPS), energy dispersive spectroscopy (EDS), transmission electron microscopy (TEM), high resolution TEM (HRTEM), scanning TEM (STEM) in high angle annular dark field mode (HAADF), and energy filtered TEM (EFTEM) using electron energy loss spectroscopy (EELS). The main goal has been to compare the structures and the physicochemical properties of the supports.

2. Experimental

2.1. Sample preparation

The samples have been prepared by the Pechini's method [25], using $Ce(NO_3)_2{\cdot}6H_2O$, $C_{12}H_{28}O_4Ti$, and $Mn(NO_3)_2{\cdot}4H_2O$ (all from Sigma–Aldrich). The precursors were dissolved in water (in the desired ratios) and stirred at 80 °C, then a solution of citric acid was added and the resulting mixture was vigorously stirred for 24 h for the polymerization to occur, and then ethylene glycol was added. The products were dried at 250 °C for 2 h, pre-calcined at 350 °C for 1 h, and calcined at 550 °C for 2 h in air. Au and Pd nanoparticles were incorporated by impregnation using $HAuCl_4{\cdot}3H_2O$ and $PdCl_2$. The samples were then calcined at 550 °C for 4 h. The prepared samples were: Au/CeO_2, Au/TiO_2, Au/Mn_2O_3, Pd/CeO_2, Pd/TiO_2, and Pd/Mn_2O_3 (0.5 at% of Au or Pd in each sample).

2.2. Characterization techniques

EDS analyses were carried out using a LEO 440 electron microscope with an Oxford detector and Link Analytical QX 2000 spectrometer. An electron beam energy of 12 eV was used.

XRD analyses were performed using a Rigaku Dmax 2500 PC diffractometer using a Cu source. The X-ray diffractograms were obtained for 2θ ranging from 20° to 70°, at a scan rate of 6 s per step, and using a power of 40 kV.

XPS spectra were acquired by a VSW HA-100 spherical analyzer using non-monochromated Al Kα radiation ($h\nu$ = 1486.6 eV). The high-resolution spectra were acquired using constant analyzer pass energy of 44 eV. The pressure inside the analysis chamber was kept below than 2×10^{-8} mbar. The powder samples were pressed into pellets and fixed to a stainless steel sample holder with double-faced conducting tape and analyzed without further preparation. Curve fitting was performed using Gaussian line shapes, and a Shirley background was subtracted from the data.

TEM analyses were performed using a Tecnai FEI G^2 F20 microscope equipped with a field emission gun (FEG) using the following image modes: high resolution TEM (HRTEM), scanning TEM (STEM) in high angle annular dark field (HAADF) using a Fischione Model 3000 detector of Z-contrast images for differentiating phases and/or elements which constitute the nanoparticles, energy filtered TEM (EFTEM) using an electron energy loss spectroscopy (EELS) Gatan image filter (GIF) Tridiem detector.

3. Results

Figs. 1–3 present the XRD diffractograms for the samples; the sharp and intense peaks indicate that the samples are highly crystalline, and the addition of Au and Pd has yielded the crystallinity unimpaired. The diffractograms for the CeO_2 substrate (bottom of Fig. 1), Pd/CeO_2 (middle of Fig. 1), and Au/CeO_2 (top of Fig. 1) showed the formation of a single crystalline ceria phase having a cubic unit cell. The addition of Au or Pd NPs has not caused

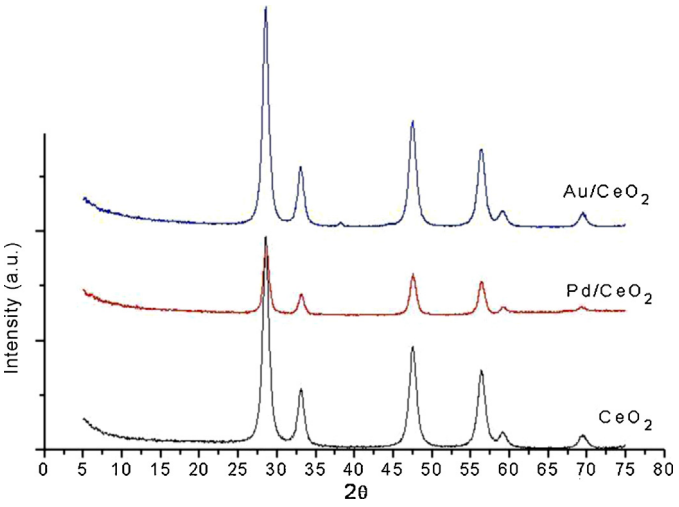

Fig. 1. DRX diffractograms for: (a) CeO_2, (b) Pd/CeO_2, and (c) Au/CeO_2.

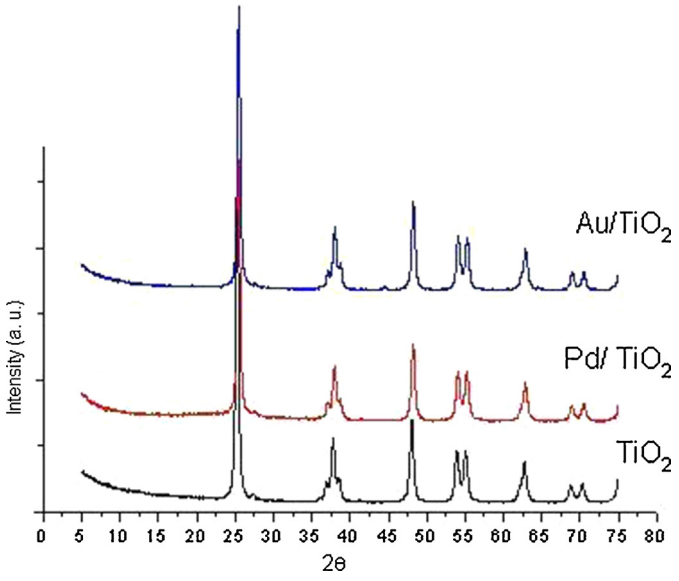

Fig. 2. DRX diffractograms for: (a) TiO_2, (b) Pd/TiO_2, and (c) Au/TiO_2.

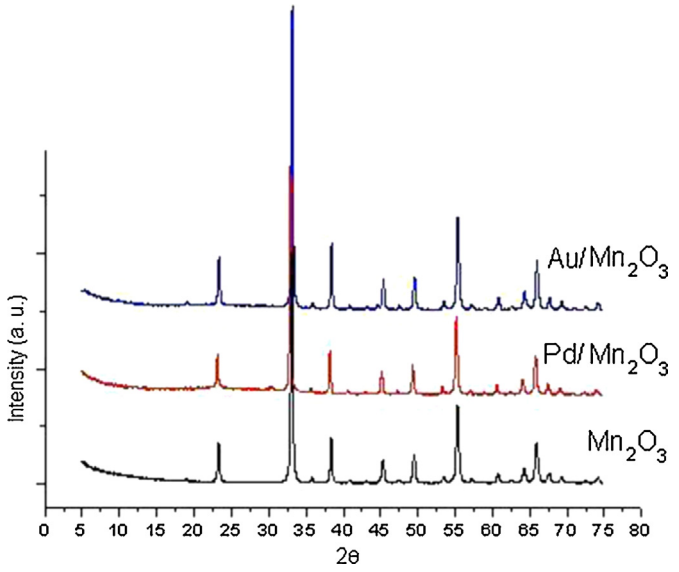

Fig. 3. DRX diffractograms for: (a) Mn_2O_3, (b) Pd/Mn_2O_3, and (c) Au/Mn_2O_3.

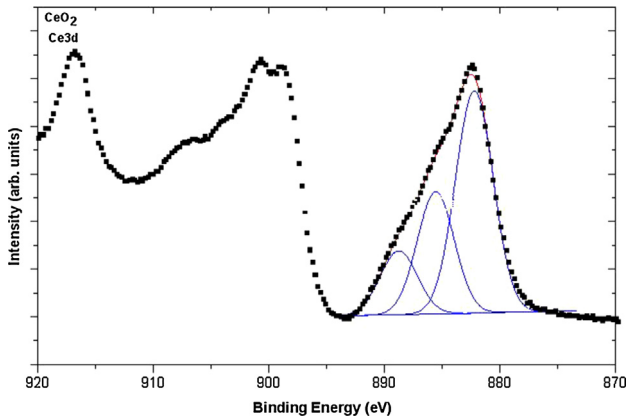

Fig. 4. XPS Ce 3d spectrum for the CeO_2 support.

the appearance of characteristic peaks associated with the dopant metal (or oxide). One possible explanation would be that both Au and Pd atoms and/or ions have been incorporated into the crystal lattice of CeO_2. Other possibility would be the formation of very small clusters of Au and Pd, and such clusters would not have defined crystalline structures, thus were not detected by XRD.

The main peaks observed in Fig. 2 correspond to a tetragonal TiO_2 (rutile) structure. As in the previous case, the addition of Au or Pd NPs has not given rise to extra peaks related to the dopant atoms and/or ions, but may have caused shifts in the peaks towards higher 2θ values for both Au/TiO_2 and Pd/TiO_2 samples, in comparison with the pure TiO_2 diffractogram. These shifts could be due to differences in the atomic and/or ionic radii of Au (0.144 nm for Au^0 and 0.137 nm for Au^{1+}) and Pd (0.137 nm for Pd^0 and 0.075 to 0.100 nm, depending on the oxidation state) compared to Ti^{4+} radius (0.064 nm).

Fig. 3 presents the XRD diffractograms for the Mn_2O_3 substrate (bottom), Pd/Mn_2O_3 (middle), and Au/Mn_2O_3 (top). The substrate peaks correspond to a cubic Mn_2O_3 structure, and the addition of Pd NPs has not caused the appearance of extra peaks related to Pd or Pd oxides, but caused a shift in the Mn_2O_3 peaks, probably due to a crystal lattice distortion. For the Au/Mn_2O_3 sample, it can be observed the appearance of a small peak at 44.6°, which is associated with gold, suggesting that the Au NPs were segregated and not incorporated into the Mn_2O_3 structure.

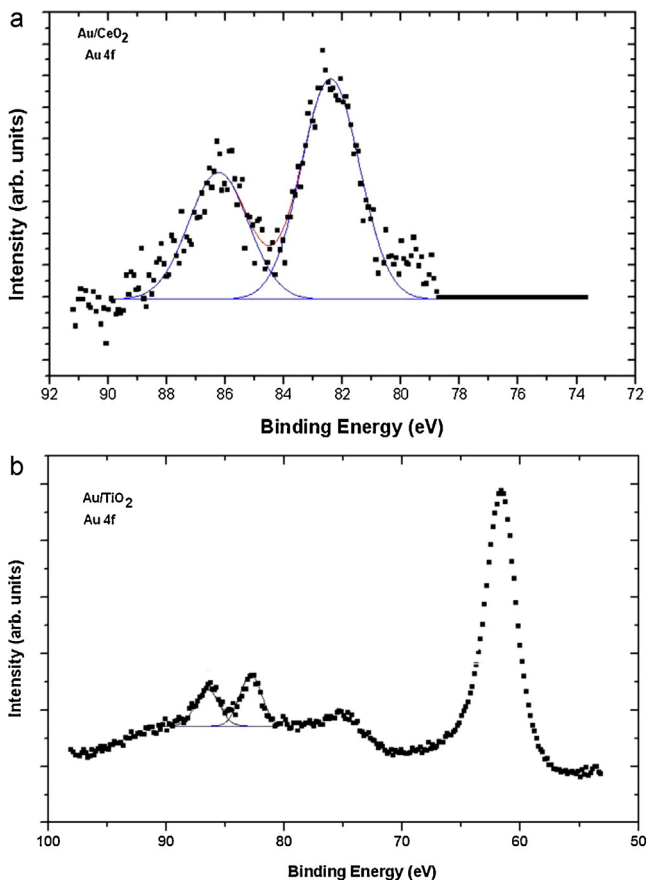

Fig. 5. XPS Au 4f spectra for: (a) Au/CeO_2 and (b) Au/TiO_2. The prominent peak at approximately 61 eV, for the Au/TiO_2 sample, corresponds to Ti 3s.

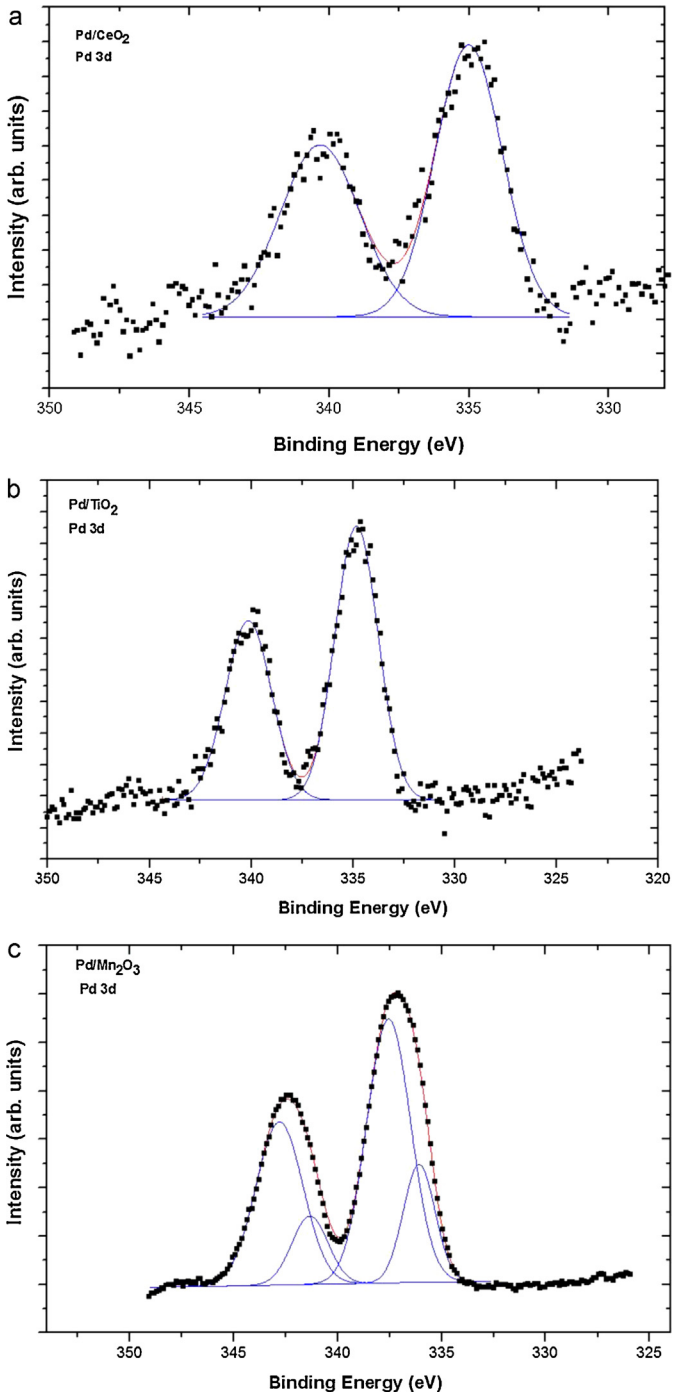

Fig. 6. XPS Pd 3d spectra for (a) Pd/CeO_2, (b) Pd/TiO_2, and (b) Pd/Mn_2O_3.

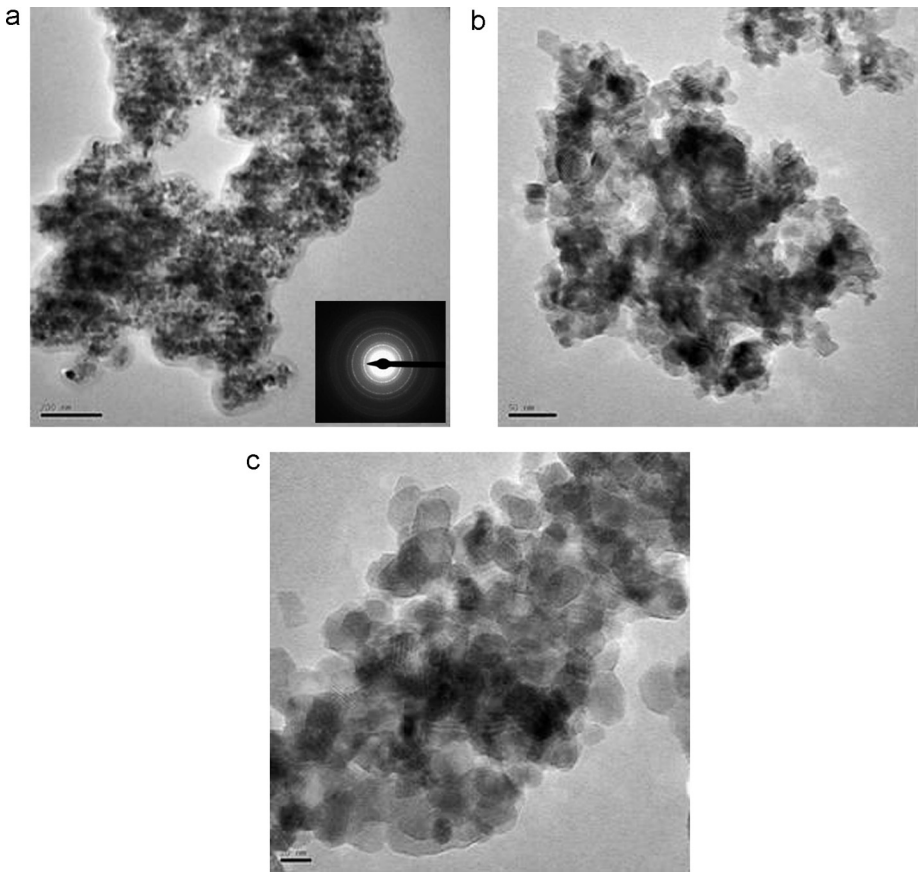

Fig. 7. Bright field (BF) TEM micrographs of (a) CeO_2, (b) Au/CeO_2, and (c) Pd/CeO_2 NPs. Selected area diffraction (SAD) pattern of CeO_2 (inset).

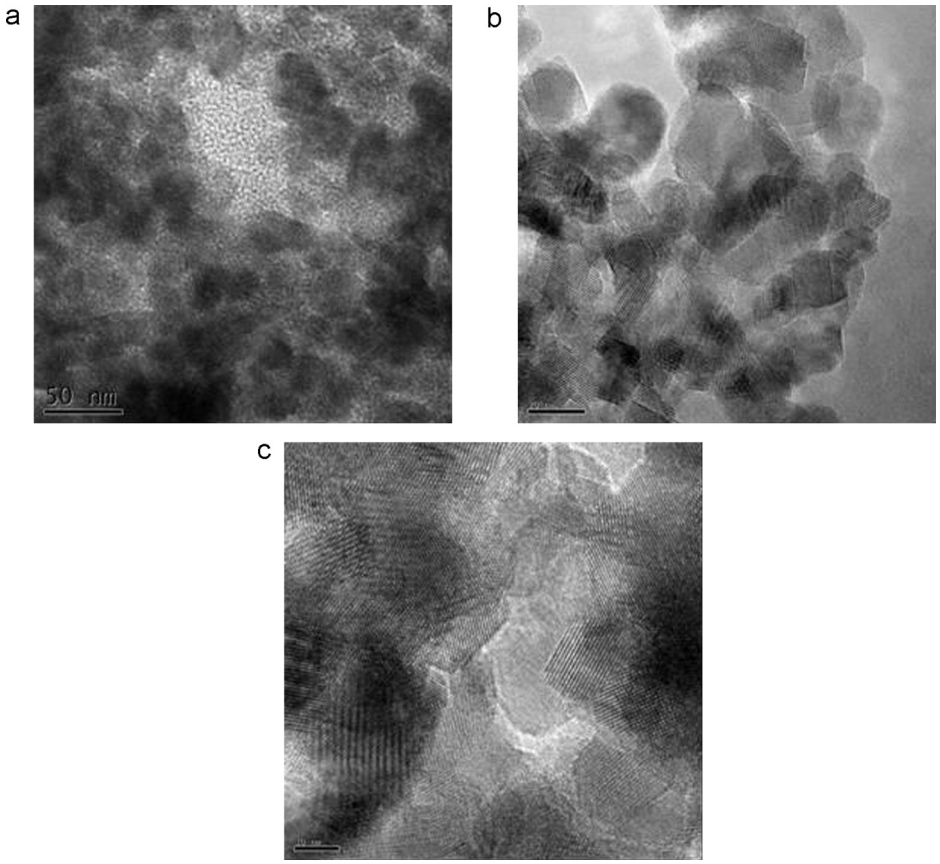

Fig. 8. HRTEM micrographs of (a) CeO_2, (b) Au/CeO_2, and (c) Pd/CeO_2 NPs.

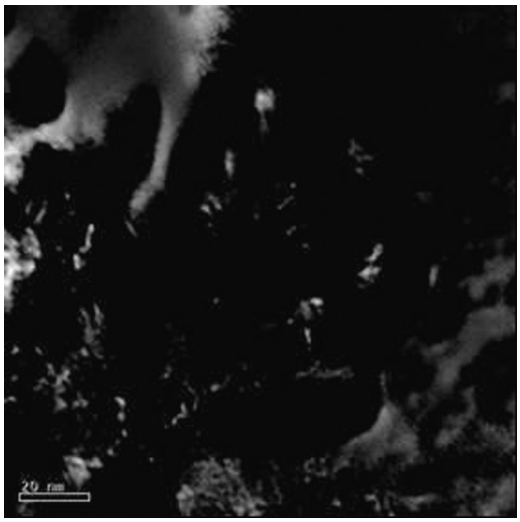

Fig. 9. Energy filtered (EF) TEM micrograph of Au/CeO_2 in Au_0 plasmon edge of 54 eV.

Fig. 4 displays the XPS Ce 3d spectrum for the CeO_2 support, which shows the typical three-lobed envelopes in the binding energy ranges of 877–892, 895–910, and 912–920 eV [26]. The first envelope was fitted with three components at 882.2, 885.5, and 889.0 eV; the components at 882.2 and 889.0 eV are ascribed to Ce^{4+} oxidation state, while the component at 885.5 eV is associated with the Ce^{3+} oxidation state [26–29]. There is a predominance of the +4 state, indicated by the main $3d_{5/2}$ component at 882.2 eV and also by a prominent peak at approximately 916.5 eV [26–29]. Francisco et al. [30] reported a 15% reduction of Ce^{4+} to Ce^{3+} due to the X-ray exposure during the XPS measurements. The addition of Au or Pd NPs did not change the Ce 3d spectrum significantly.

Fig. 5 displays the XPS Au 4f spectra for (a) Au/CeO_2 and (b) Au/TiO_2. It was not possible to obtain an Au 4f spectrum for Au/Mn_2O_3 due to an overlap with the Mn 3p spectrum. The prominent peak at approximately 61 eV for Au/TiO_2 corresponds to Ti 3s. The measured Au $4f_{7/2}$ binding energy for Au/CeO_2 and Au/TiO_2 are lower (82.4 and 82.8 eV, respectively) than the value for pure gold (84.0 eV). There are very few reports on the literature regarding such negative shift and there is no consensus about it. Au $4f_{7/2}$ binding energies below or equal to 83.0 eV for Au NPs dispersed on TiO_2 were reported by Radnik et al. [31], Arrii et al. [32], and Hao et al. [33]. These negative shifts could be due to the electronic state of the Au NPs, particle size effects, or different structural arrangements [31]. Some authors have attributed these negative shifts to a strong metal-support interaction [32,33]. Apostol et al. [34] reported lower Au $4f_{7/2}$ binding energies (around 81.4 eV) for Au thin layers (0.2–4 nm) deposited on $Pb(Zr,Ti)O_3$ (PZT), and they attributed such low values to negatively charged gold organized in clusters or NPs, which are insulated from the ground and charged by the PZT [34].

Liu et al. [35] associated the negative shift of Au 4f binding energies for Au-Pd NPs (Au core–Pd shell) to an increase in the surface to volume ratio as the Au core became smaller. Sham et al. [36] reported a XPS investigation on thiol-capped Au NPs which showed a metallic to non-metallic transition as the average Au NP size decreased. They estimated a value of $\sim 1.7 \pm 0.3$ eV for the pseudo-gap for the Au NPs having a size of approximately 1.5 nm. A similar size-induced metal-insulator transition could account for the low Au 4f binding energies observed in this work for Au/CeO_2 and Au/TiO_2.

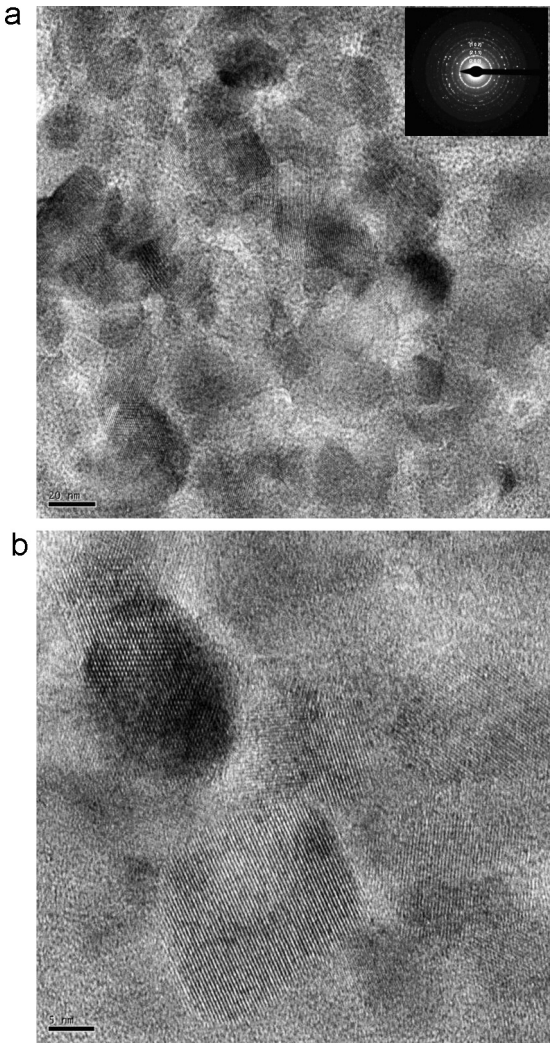

Fig. 10. TEM micrographs for the TiO_2 support sample: (a) BF mode with the respective SAD ring pattern and (b) HRTEM showing the planes and atomic positions of the TiO_2 NPs with different morphologies.

Fig. 6 displays the XPS Pd 3d spectra for (a) Pd/CeO_2, (b) Pd/TiO_2, and (c) Pd/Mn_2O_3. For the Pd NPs on both CeO_2 and TiO_2 supports, the Pd 3d doublet was fitted using only one component for each of the spin–orbit peaks, $3d_{5/2}$ and $3d_{3/2}$. The Pd $3d_{5/2}$ binding energy of 335.0 eV corresponds to metallic Pd [37,38]. For the Mn_2O_3 support, there are two components for each of the spin–orbit peaks, with Pd $3d_{5/2}$ at 336.1 eV (24% of the total peak area) and 337.5 eV (76% of the total peak area), which can be attributed to PdO and PdO_2, respectively [39–42]. Kibis et al. [42] proposed that the Pd NPs possess a mixture of PdO and PdO_2 oxides, and that the Pd^{4+} state is stabilized by the PdO oxide.

Fig. 7 displays bright field (BF) TEM micrographs of (a) CeO_2, (b) Au/CeO_2, and (c) Pd/CeO_2 NPs; the inset is a selected area diffraction (SAD) pattern of CeO_2. It can be observed the formation of ceria nanocrystals. Fig. 8 shows HRTEM micrographs of (a) CeO_2, (b) Au/CeO_2, and (c) Pd/CeO_2 NPs. While palladium was dispersed homogeneously on the CeO_2 support, gold formed clusters in between the CeO_2 NPs ($\sim$30 nm). Fig. 9 shows TEM micrograph in energy filtered mode (EFTEM) using a GIF detector in the plasmon edge energy of 54 eV (Au_0 edge), confirming that Au formed clusters in between the CeO_2 NPs. The small cluster sizes could explain why Au was not detected by XRD.

Fig. 10 displays typical TEM micrographs of the TiO_2 support. The BF mode micrograph depicted in Fig. 10(a) shows the

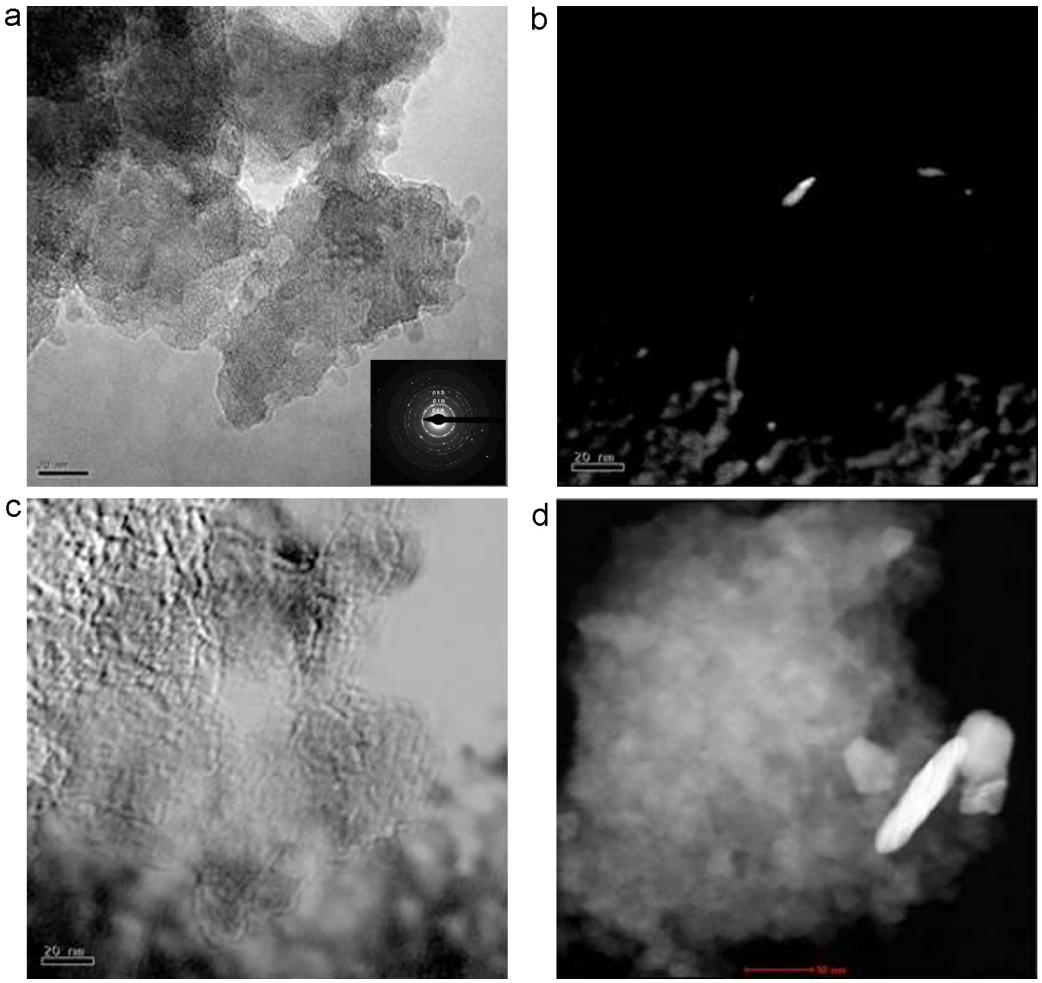

Fig. 11. Micrographs for the Au/TiO_2 sample: (a) BF TEM image with the respective SAD pattern; (b) EFTEM micrograph obtained in the plasmon edge energy of 54 eV (Au_O edge); (c) EFTEM image obtained in the plasmon edge energy of 35 eV (Ti_M edge); and (d) STEM image acquired with a HAADF detector showing Au NPs distributed in the TiO_2 support.

distribution of the TiO_2 NPs, and the respective SAD ring pattern in the inset denotes a nanocrystalline distribution of these TiO_2 NPs. Fig. 10(b) presents the HRTEM micrograph in a higher magnification showing details of the TiO_2 NPs having different morphologies, with particle sizes ranging from 10 to 40 nm. The TiO_2 structure was identified as being rutile (tetragonal), having d_{200}, d_{211}, and d_{102} interplanar distances of 4.80, 3.44, and 2.65 Å, respectively.

Fig. 11(a) displays a TEM micrograph in BF mode for the Au/TiO_2 sample and the respective SAD pattern, typical of a nanocrystalline

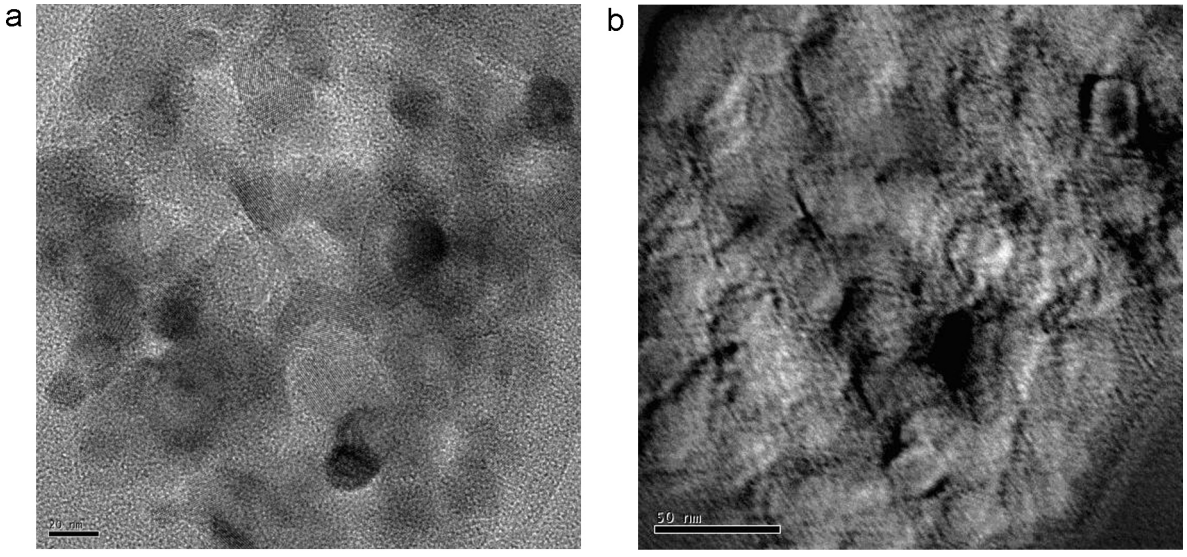

Fig. 12. TEM micrographs for the Pd/TiO_2 sample: (a) BF mode image and (b) EFTEM image obtained in the plasmon edge energy of 51 eV (Pd_N edge).

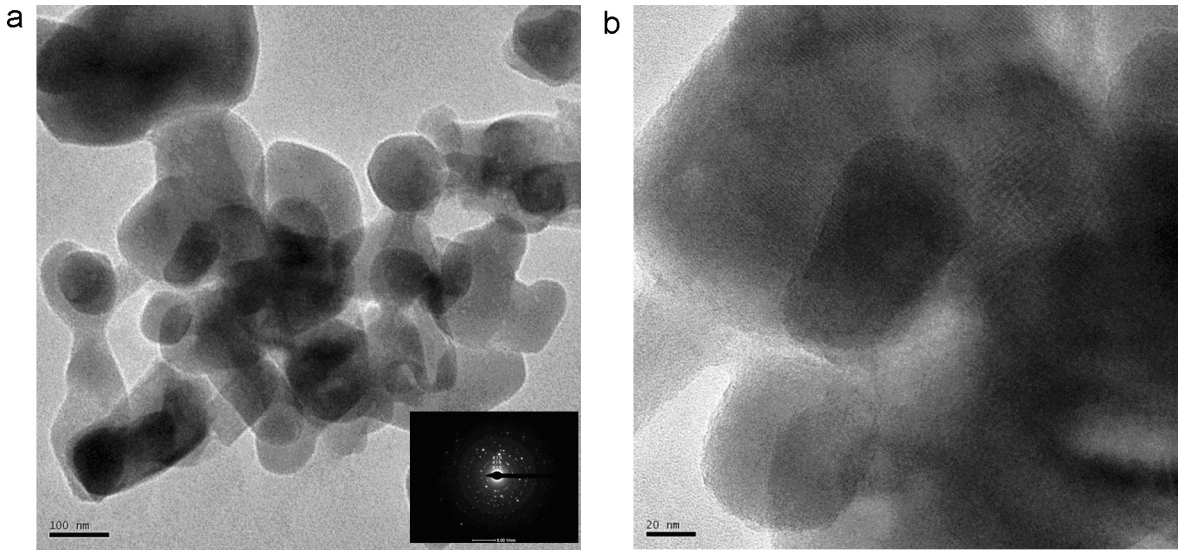

Fig. 13. TEM micrographs for the nanostructured Mn_2O_3 support: (a) BF mode with the respective SAD pattern and (b) HRTEM showing in detail the crystalline planes of the Mn_2O_3 NPs with distinct morphologies.

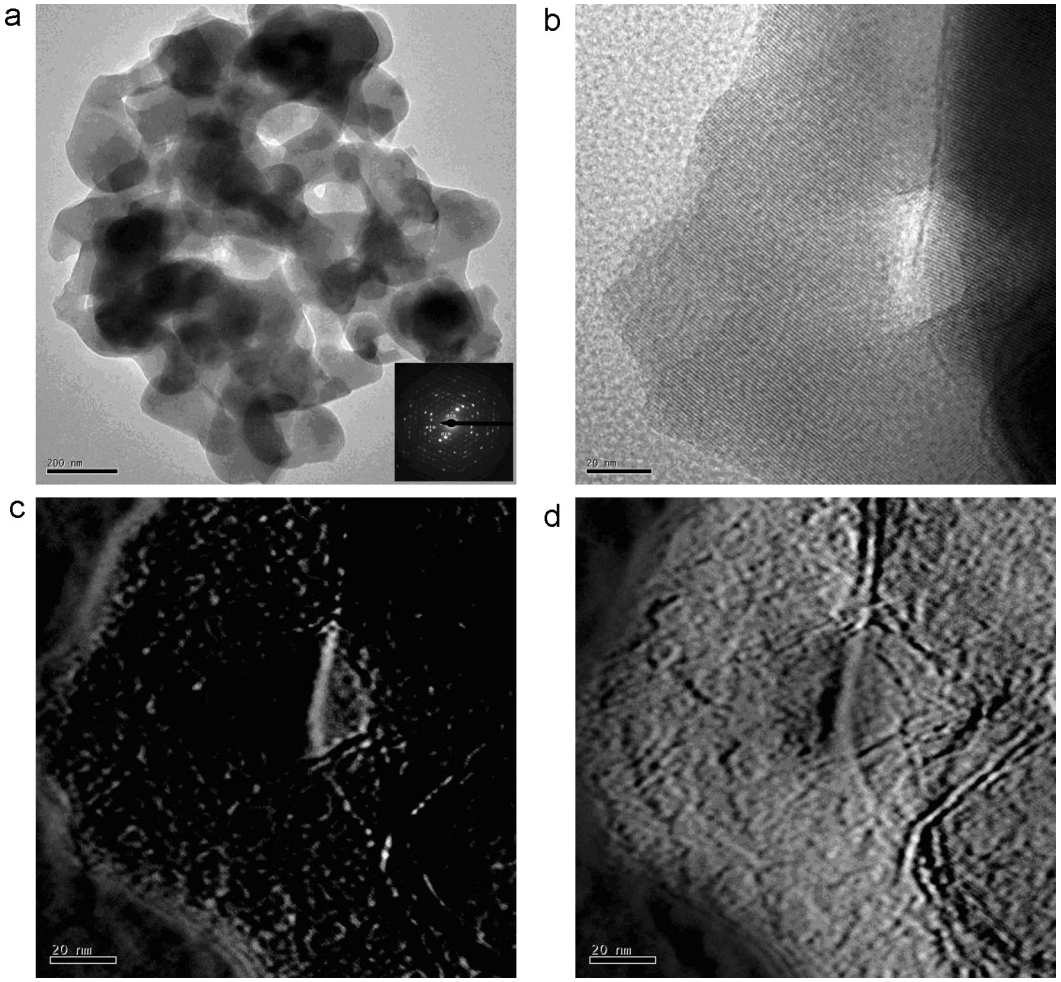

Fig. 14. Micrographs for the Au/Mn_2O_3 sample: (a) BF TEM image with the respective SAD pattern; (b) HRTEM image showing the crystalline planes of the Mn_2O_3 nanograins; (c) EFTEM image obtained in the plasmon edge energy of 54 eV (Au_O edge) showing Au clusters; and (d) EFTEM image obtained in the plasmon edge energy of 24.8 eV (Mn_M edge).

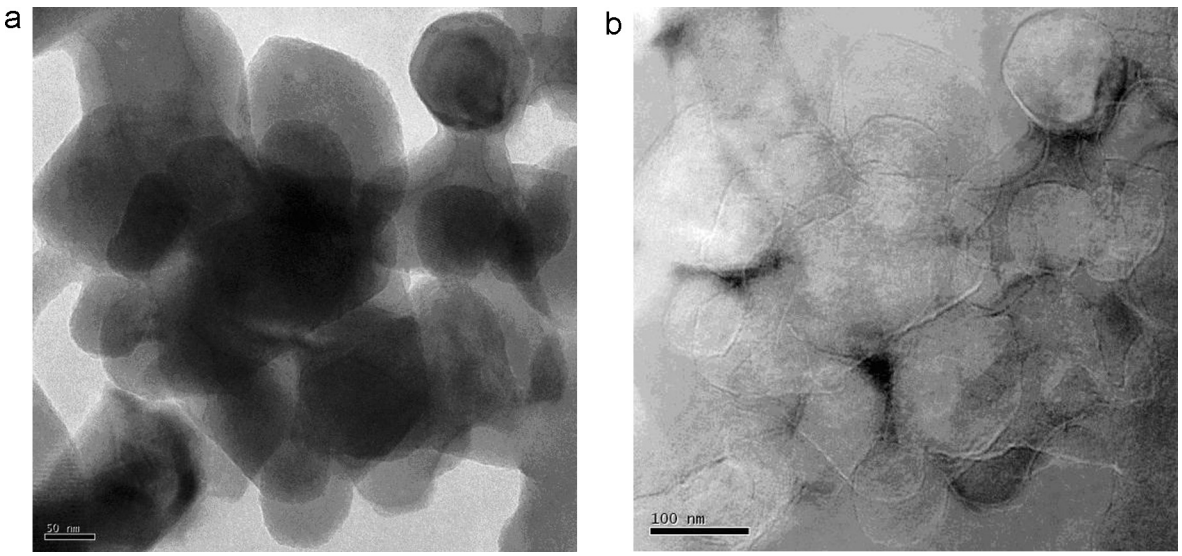

Fig. 15. Micrographs for the Pd/Mn_2O_3 sample: (a) BF TEM image and (b) EFTEM image obtained in the plasmon edge energy of 51 eV (Pd_N edge).

structure. Fig. 11(b) displays an EFTEM micrograph in the plasmon edge energy of 54 eV (Au_O edge), showing a heterogeneous distribution of the Au NPs throughout the TiO_2 NPs support. Fig. 11(c) presents an EFTEM micrograph of the Ti distribution by using the plasmon energy of 35 eV (Ti_M edge), and Fig. 11(d) displays a STEM micrograph acquired with a high angle annular dark field (HAADF) detector, showing a heterogeneous distribution of Au agglomerates with sizes ranging from 50 to 100 nm. Ismail et al. [43] reported that a sample of 0.5 wt% Au deposited onto mesoporous TiO_2 had particle sizes for the Au NPs ranging from 5 to 10 nm. The difference among their and our results lies on the different synthesis routes that were employed. The use of mesoporous TiO_2 as support had the effect of incorporating Au NPs with smaller sizes [43].

Fig. 12(a) shows a BF TEM micrograph for Pd/TiO_2 sample and Fig. 12(b) shows an EFTEM obtained in the plasmon edge energy of 51 eV (Pd_N edge), indicating that palladium is distributed homogeneously throughout the TiO_2 support. This result is in agreement with a TEM analysis carried out by Suttiponparnit et al. [44] that showed no clear formation of Pd NPs for a sample of 1 wt% Pd incorporated onto TiO_2 NPs. An EDS spectrum (not shown here), which was collected from an agglomerate shown in Fig. 12(a), confirmed the presence of Pd incorporated onto the nanostructured TiO_2 support.

Fig. 13(a) displays a TEM micrograph obtained in BF mode of the nanostructured Mn_2O_3 support with the respective SAD pattern, which reveals that the Mn_2O_3 NPs have sizes in the range of 50 to 200 nm. Fig. 13(b) displays a HRTEM micrograph of the Mn_2O_3 support showing its crystalline planes, which are consistent with a BCC phase having d_{211}, d_{200}, and d_{231} interplanar distances of 4.98, 3.30, and 2.47 Å, respectively.

Fig. 14(a) displays a BF TEM micrograph for the Au/Mn_2O_3 sample and the inset depicts the respective SAD pattern, which is characteristic of a nanocrystalline structure. Fig. 14(b) displays a HRTEM micrograph in higher magnification showing the crystalline planes and atomic columns of the Mn_2O_3 nanograins, having a BCC phase with d_{211}, d_{222}, and d_{422} interplanar distances of 3.98, 2.80, and 1.95 Å, respectively. Fig. 14(c) displays an EFTEM micrograph obtained in the plasmon edge energy of 54 eV (Au_O edge) showing a heterogeneous and very fine distribution of the Au clusters (ranging from 1 to 5 nm) throughout the Mn_2O_3 support. Fig. 14(d)

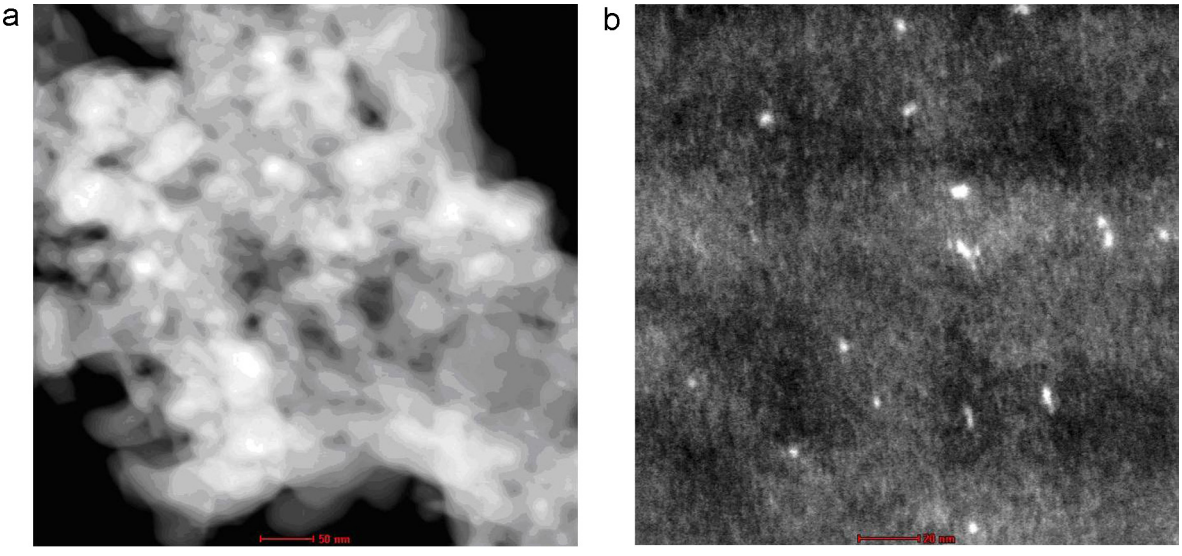

Fig. 16. (a) Low magnification and (b) high magnification STEM micrographs obtained with HAADF detector (Z contrast) for the Pd/Mn_2O_3 sample showing very fine Pd clusters.

displays an EFTEM micrograph obtained in the plasmon edge energy of 24.8 eV (Mn_M edge). An EDS spectrum (not shown here), which was collected from an agglomerate shown in Fig. 14(a), confirmed the presence of Au incorporated onto the Mn_2O_3 support.

Fig. 15(a) displays a TEM micrograph obtained in BF mode for the Pd/Mn_2O_3 sample and Fig. 15(b) displays an EFTEM micrograph in the plasmon edgy energy of 51 eV (Pd_N edge), showing a homogeneous distribution of Pd throughout the Mn_2O_3 NPs support (sizes around 100 nm). Fig. 16 displays (a) low magnification and (b) high magnification STEM micrographs obtained with HAADF detector (proportional to Z contrast) for the Pd/Mn_2O_3 sample. Fig. 16(b) exhibits the distribution of very small agglomerates (clusters) of Pd, with sizes ranging from 1 to 4 nm, which are distributed through the Mn_2O_3 nanograins. Such small cluster sizes could explain why Pd was not detected by XRD.

4. Conclusions

Half an atomic percent of Au and Pd NPs were incorporated onto CeO_2, TiO_2, and Mn_2O_3 supports and then were investigated by XRD, XPS, EDS, TEM, HRTEM, STEM, and EFTEM.

XRD characterization indicates that the CeO_2 support had a cubic structure and the addition of either Au or Pd caused negligible lattice changes. The TiO_2 support had a tetragonal (rutile) TiO_2 structure and the addition of either Au or Pd caused a distortion in the lattice. The Mn_2O_3 support had a cubic structure. On one hand, XRD results on the addition of Pd NPs indicate that they were incorporated into the cubic Mn_2O_3 structure and caused a crystal lattice distortion. On the other hand, XRD results on the addition of Au NPs indicate that they were segregated and not incorporated into the cubic Mn_2O_3 structure.

XPS results indicate that the Pd NPs on both CeO_2 and TiO_2 supports were in the metallic state, while the Pd NPs on Mn_2O_3 were oxidized. A negative chemical shift for the Au 4f doublet has been observed for both CeO_2 and TiO_2 supports and could be attributed to a size-induced metal-insulator transition for the Au NPs.

TEM analyses confirmed that additions of 0.5 wt% of Au and Pd did not change the size of CeO_2, TiO_2, and Mn_2O_3 NPs. The comparison of the additions of Au to the three different supports showed that the Au dispersion is different, with the formation of Au clusters in between the CeO_2 NPS, formation of Au NPs for the TiO_2 support, and homogeneous distribution of Au clusters for the Mn_2O_3 support. Also the additions of Pd to CeO_2, TiO_2, and Mn_2O_3 supports showed some differences, with no noticeable formation of Pd NPs or clusters for either CeO_2 or TiO_2 supports, and a very fine distribution of Pd clusters for the Mn_2O_3 support.

Acknowledgments

Grants and scholarship from the Brazilian agencies FAPESP (processes 2010/1793-2 and 2007/54829-5) and CNPq are gratefully acknowledged. We would like to thank Prof. Corinne Arrouvel (Federal University of Sao Carlos, Sorocaba Campus, Brazil) for her comments, Madalena Turssi (Federal University of Sao Carlos, Sao Carlos Campus, Brazil) for the XRD measurements, Rita C. G. Vinhas (State University of Campinas, Campinas Campus, Brazil) for the XPS measurements, and Ana Clara Stenico (Federal University of Sao Carlos, Sao Carlos Campus, Brazil) for the XPS figures.

References

[1] G.A. Somorjai, Introduction to Surface Chemistry and Catalysis, Wiley Publishers, New York, 1994.
[2] C.C. Chusuei, X. Lai, K. Luo, D.W. Goodman, Top. Catal. 14 (2001) 71–83.
[3] D.K. Kim, Y. Zhang, J. Kehr, T. Klason, B. Bjelke, M. Muhammed, J. Magn. Magn. Mater. 225 (2001) 256–261.
[4] B. O'Regan, M. Grätzel, Nature 353 (1991) 737–740.
[5] E.R. Stobbe, B.A. de Boer, J.W. Geus, Catal. Today 47 (1999) 161–167.
[6] Q. Fu, H. Saltsburg, M. Flytzani-Stephanopoulos, Science 301 (2003) 935–938.
[7] A. Karpenko, R. Leppelt, V. Plzak, J. Cai, A. Chuvilin, B. Schumacher, U. Kaiser, R.J. Behm, Top. Catal. 44 (2007) 183–198.
[8] H. Liang, J.M. Raitano, G. He, A.J. Akey, I.P. Herman, L. Zhang, S.W. Chan, J. Mater. Sci. 47 (2012) 299–307.
[9] M. Hosseini, S. Siffert, H.L. Tidahy, R. Cousin, J.F. Lamonier, A. Aboukais, A. Vantomme, M. Roussel, B.L. Su, Catal. Today 122 (2007) 391–396.
[10] C. Zhang, H. He, Catal. Today 126 (2007) 345–350.
[11] V. Mendez, V. Caps, S. Daniele, Chem. Commun. 21 (2009) 3116–3118.
[12] X.B. Li, E. Iglesia, Angew. Chem. Int. Ed. 46 (2007) 8649–8652.
[13] J. Hong, W. Chu, M. Chen, X. Wang, T. Zhang, Catal. Commun. 8 (2007) 593–597.
[14] N.J. Coulston, R.P.K. Wells, P.B. Wells, G.J. Hutchings, Catal. Today 114 (2006) 353–356.
[15] P. Weerachawanasak, P. Praserthdam, M. Arai, J. Panpranot, J. Mol. Catal. A 279 (2008) 133–139.
[16] M.V. Rahaman, M.A. Vannice, J. Catal. 127 (1991) 251–266.
[17] K. Ramesh, L. Chen, F. Chen, Z. Zhong, J. Chin, H. Mook, Y.F. Han, Catal. Commun. 8 (2007) 1421–1426.
[18] Y.F. Han, L. Chen, K. Ramesh, E. Widjaja, S. Chilukoti, I.K. Surjami, J. Chen, J. Catal. 253 (2008) 261–268.
[19] K. Frey, V. Iablokov, G. Safran, J. Osan, I. Sajo, R. Szukiewicz, S. Chenakin, N. Kruse, J. Catal. 287 (2012) 30–36.
[20] B. Hammer, J.K. Norskov, Nature 376 (1995) 238–240.
[21] M. Haruta, Catal. Today 36 (1997) 153–166.
[22] M. Haruta, T. Kobayashi, H. Sano, N. Yamada, Chem. Lett. (1987) 405–408.
[23] M. Haruta, N. Yamada, T. Kobayashi, S. Iijima, J. Catal. 115 (1989) 301–309.
[24] M. Haruta, Chem. Rec. 3 (2003) 75–87.
[25] E.R. Leite, I.T. Weber, E. Longo, J.A. Varela, Adv. Mater. 12 (2000) 965–968.
[26] F. Larachi, J. Pierre, A. Adnot, A. Bernis, Appl. Surf. Sci. 195 (2002) 246–250.
[27] M. Romeo, K. Bak, J. Elfallah, F. Lenormand, L. Hilaire, Surf. Interface Anal. 20 (1993) 508–512.
[28] A. Trovarelli, Catal. Rev. 38 (1996) 439–520.
[29] D.R. Mullins, S.H. Overbury, D.R. Huntley, Surf. Sci. 409 (1998) 307–319.
[30] M.S.P. Francisco, V.R. Mastelaro, P.A.P. Nascente, A.O. Florentino, J. Phys. Chem. B 105 (2001) 10515–10522.
[31] J. Radnik, C. Mohr, P. Claus, Phys. Chem. Chem. Phys. 5 (1) (2003) 172–177.
[32] S. Arrii, F. Morfin, A.J. Renouprez, J.L. Rousset, J. Am. Chem. Soc. 126 (2004) 1199–1205.
[33] Y. Hao, R. Liu, X. Meng, H. Cheng, F. Zhao, J. Mol. Catal. A 335 (2011) 183–188.
[34] N.G. Apostol, L.E. Stoflea, G.A. Lungu, C. Chirila, L. Trupina, R.F. Negrea, C. Ghica, L. Pintilie, C.M. Teodorescu, Appl. Surf. Sci. 273 (2013) 415–425.
[35] F. Liu, D. Wechsler, P. Zhang, Chem. Phys. Lett. 461 (2008) 254–259.
[36] T.K. Sham, P.-S.G. Kim, P. Zhang, Sol. State Commun. 138 (2006) 553–557.
[37] M.C. Militello, S.J. Simko, Surf. Sci. Spectra 3 (1994) 387–394.
[38] G. Cristoforetti, E. Pitzalis, R. Spiniello, R. Ishak, F. Giammanco, M. Muniz-Miranda, S. Caporali, Appl. Surf. Sci. 258 (2012) 3289–3297.
[39] M. Brun, A. Berthet, J.C. Bertolini, J. Electron Spectrosc. Relat. Phenom. 104 (1999) 55–60.
[40] Y. Sohn, D. Pradhan, K.T. Leung, ACS Nano 4 (2010) 5111–5120.
[41] W.-Y. Huang, S.-J. Ding, H.-B. Chen, Q.-Q. Sun, D.W. Zhang, J. Vac. Sci. Technol. A 29 (2011) 021006.
[42] L.S. Kibis, A.I. Stadnichenko, S.V. Koscheev, V.I. Zaikovskii, A.I. Boronin, J. Phys. Chem. C 116 (2012) 19342–19348.
[43] A.A. Ismail, S.A. Al-Sayari, D.W. Bahnemann, Catal. Today 209 (2013) 2–7.
[44] K. Suttiponparnit, V. Tiwari, M. Sahu, P. Biswas, S. Suvachittanont, T. Charinpanitkul, J. Ind. Eng. Chem. 19 (2013) 150–156.